Programmable viscosity metamaterials: Designing fluid properties using temporal superposition of shear and acoustics

Prateek Sehgal [1,*] Meera Ramaswamy [2] Edward Y. X. Ong [2] Christopher Ness [3] Itai Cohen [2] and Brian J. Kirby [1,4]

[1] *Sibley School of Mechanical and Aerospace Engineering, Cornell University, Ithaca, New York 14853, USA*

[2] *Department of Physics, Cornell University, Ithaca, New York 14853, USA*

[3] *School of Engineering, University of Edinburgh, Edinburgh EH9 3FG, United Kingdom*

[4] *Department of Medicine, Division of Hematology and Medical Oncology, Weill–Cornell Medicine, New York, New York 10021, USA*

(Received 1 August 2023; accepted 22 September 2024; published 5 November 2024)

Metamaterials are composite structures whose extraordinary properties arise from a mesoscale organization of their constituents. Here, we introduce a different material class—viscosity metafluids. Specifically, we demonstrate that we can rapidly drive large viscosity oscillations in shear-thickened fluids using acoustic perturbations with kHz to MHz frequencies. Because the timescale for these oscillations can be orders of magnitude smaller than the timescales associated with the global material flow, we can construct metafluids whose resulting time-averaged viscosity is a composite of the thickened, high-viscosity and dethickened, low-viscosity states. We show that viscosity metafluids can be used to engineer a variety of unique properties including zero, infinite, and negative viscosities. The high degree of control over the resulting viscosity, the ease with which they can be accessed, and the variety of exotic properties achievable make viscosity metafluids attractive for uses in technologies ranging from coatings to cloaking to 3D printing.

DOI: 10.1103/PhysRevResearch.6.043107

I. INTRODUCTION

Metamaterials have been used to engineer exotic properties that are otherwise impossible to achieve with conventional materials, including negative indexes of refraction, perfect absorption of electromagnetic radiation, and negative Poisson ratios [1–9]. More recently, properties such as multistability [10], programmable compressibility [11], and negative refractive index [12] have been achieved in *metafluids*, where specially engineered particles are suspended within a Newtonian fluid. Here, we propose to create a different class of metafluids—viscosity metafluids—by temporally organizing the fluidic building blocks of an otherwise conventional suspension. Our inspiration for designing viscosity metafluids arises from the tunability of a shear-thickened suspension's viscosity via acoustic perturbations [13]. Under shear, nearly all dense suspensions undergo a thickening transition from a low-viscosity to a high-viscosity state [14–17]. This transition occurs when the applied shear stresses are large enough to drive particles into contact, forming force chains that are primarily aligned along the maximum compressive axis [18–32]. The resulting increase in viscosity can span orders of magnitude and in sufficiently dense suspensions can result in a completely rigid, shear jammed state. Recently, we have shown that by applying acoustic perturbations the suspension viscosity can be tuned from the thickened to the fully dethickened state [13]. The applied acoustic perturbations are presumed to dethicken the suspension by breaking up particle contacts important for force transduction. While our previous study focused on applying static and quasistatic acoustic perturbations, we found that the suspension response occurred on the millisecond timescale. This fast response time coupled with the ease with which the acoustic field can be manipulated indicates that there is an opportunity to generate tunable material properties via rapidly cycling between the thickened and dethickened states (Fig. 1).

We pursue this strategy using charge stabilized monodispersed colloidal suspensions consisting of 2-μm silica particles suspended in dipropylene glycol ($\eta_0 = 0.11$ Pa s) at a volume fraction of $\phi \simeq 0.53$. When we apply acoustic perturbations to a quiescent suspension (for apparatus and analysis, see Methods), we find that particles form a disordered hyperuniform state, as shown by the behavior of the number density variance and structure factor in Fig. 1(a). These results indicate that acoustic perturbations generate isotropic repulsion that maximizes the interparticle separations as shown in the schematic at the bottom of Fig. 1(a). Conversely, as the suspension thickens under shear, particles form contacts, organized into anisotropic force chains that align with the maximum compressive axis. The increase in viscosity arises from the increase in average number of contacts between the particles [19,28,30,33] [Fig. 1(b)]. In simulations {see Appendix 2 and Supplemental Material (SM) [34] and Ref. [35] therein for details}, the force chains formed can be visualized by plotting the three-dimensional microstructure as seen in the inset of Fig. 1(b). These results illustrate that there

*Contact author: ps824@cornell.edu

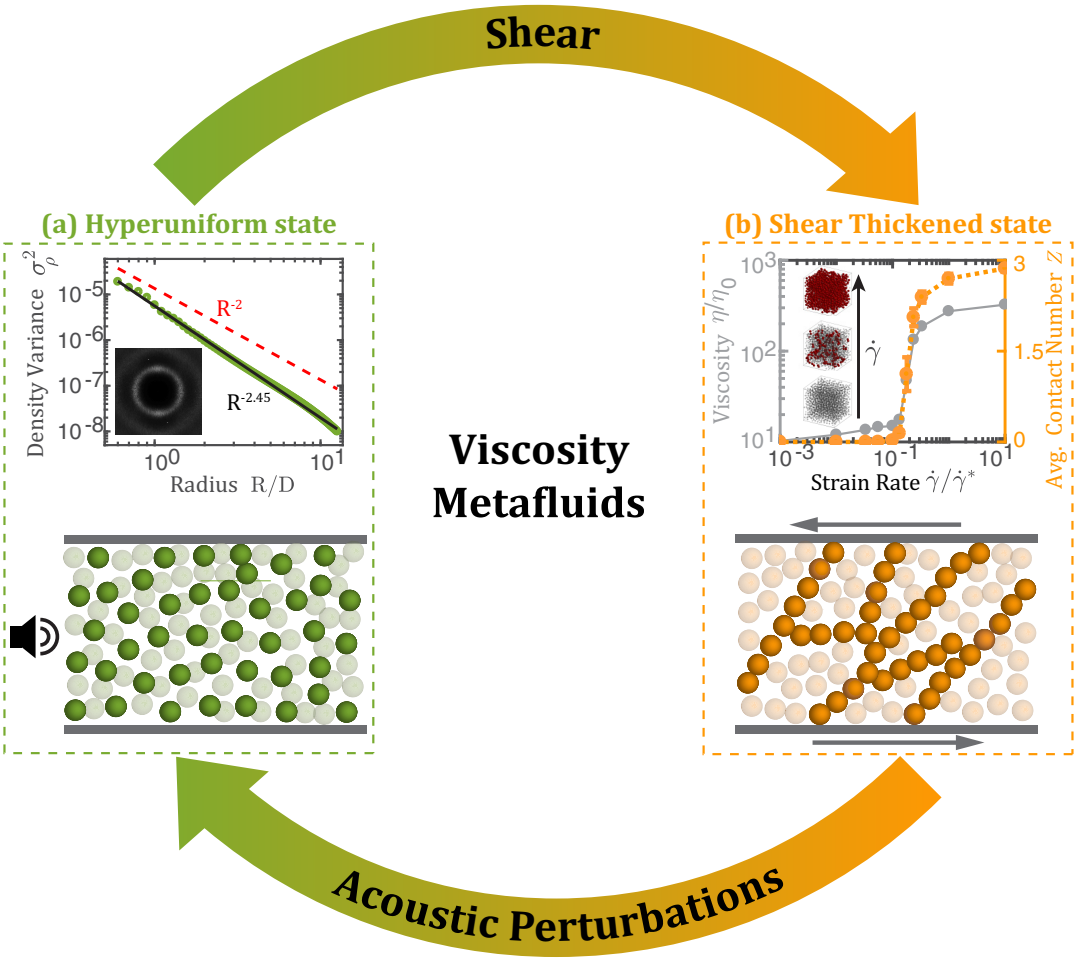

FIG. 1. Viscosity metafluids generated by the interplay of acoustic perturbations and applied shear. (a) (Top) Evolution of number density variance σ_ρ^2 (green circles) with radius R/D of the observation window in the presence of acoustic perturbations. Here, D is the particle diameter and red-dashed line shows R^{-2} scaling of a completely random system for reference. σ_ρ^2 decays faster than R^{-2} and approximately scales with $R^{-2.45}$ (solid-black line), which is similar to the exponent observed for hyperuniform absorbing states at criticality [36,37]. (Inset) The spectrum of structure factor $S(\mathbf{k})$, with $\mathbf{k} = 0$ at the center. Forward scattering, i.e., $S(\mathbf{k} = 0)$, is omitted from the spectrum. $S(\mathbf{k})$ exhibits a dark region in the center (at small k) surrounded by a bright ring. The behavior of both σ_ρ^2 and $S(\mathbf{k})$ are hallmarks of disordered hyperuniform states [38–41]. The data is obtained from the average of over 1200 images from the timelapse. (Bottom) Schematic representation of the hyperuniform arrangement of particles in the presence of acoustic perturbations. (b) (Top) Flow curve showing suspension viscosity η/η_0 (left axis) and contact number Z (right axis) as functions of shear rate $\dot{\gamma}/\dot{\gamma}^*$ obtained from particle-based simulation (see Appendix). (Inset) Snapshots of the suspension microstructures at increasing shear rate. Particles in red have at least one contacting particle while those in grey have none. We observe formation of the force chains with increasing shear rate. (Bottom) Schematic representation of the force chain network in a shear-thickened state. (Large circular arrows) Toggling between the hyperuniform state and shear thickened state allows for generating viscosity metafluids.

is an opportunity for toggling between these two structural arrangements to form viscosity metafluids.

II. RESULTS

A. Generating viscosity metafluids using intermittent acoustic perturbations

Here, we show how we can temporally structure acoustic perturbations on the millisecond timescale to generate metafluid states in colloidal suspensions. We develop acoustic protocols and implement them using a previously described acoustic apparatus mounted on an Anton Paar MCR Rheometer [13]. In particular, to generate oscillations in the viscosity, we apply the acoustic fields intermittently. We anticipate that over the period where the acoustic perturbations are on T_{on}, the viscosity will rapidly drop because of dissolution of force chains. Conversely, over the period where the perturbations are turned off T_{off}, formation of force chains is unimpeded, and the viscosity increases.

The response of the suspension sheared at $\dot{\gamma} = 0.44\,\text{s}^{-1}$ to our acoustic protocols is shown in Figs. 2(a) and 2(b). Under steady shear with no applied acoustic perturbations, the suspension maintains a shear-thickened viscosity [yellow region in Figs. 2(a) and 2(b)]. Application of continuous acoustic perturbations at 1.15 MHz, 5 V partially dethickens the suspension [light green region in Figs. 2(a) and 2(b)]. Toggling these perturbations on and off with $T_{\text{on}} = 0.5\,\text{s}$ and $T_{\text{off}} = 0.5\,\text{s}$ results in rapid oscillations between the fully thickened

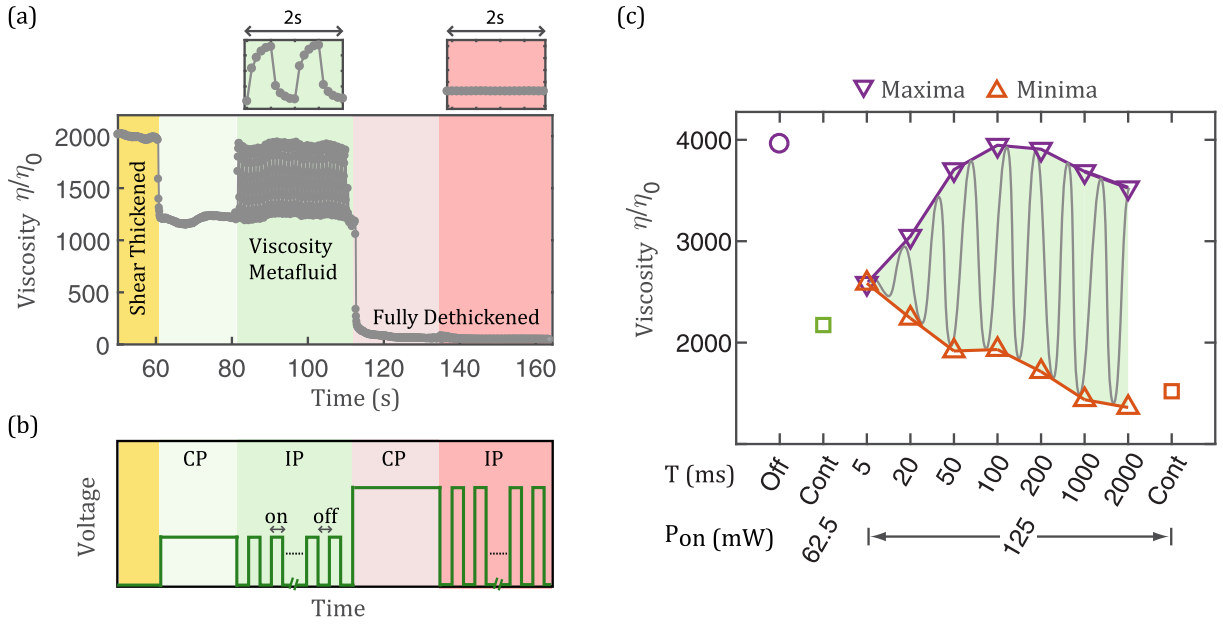

FIG. 2. Generating viscosity metafluids by use of shear and intermittent acoustic perturbations. (a) Instantaneous viscosity response of the suspension to the continuous perturbations (CP) and intermittent perturbations (IP). Here, η_0 is the solvent viscosity (dipropylene glycol, 0.11 Pa s). The measurement is performed at a steady strain rate of $\dot{\gamma} = 0.44\ \mathrm{s}^{-1}$. The suspension maintains a shear-thickened state for the first 60 s. After thickening, the suspension is partially dethickened by applying 3 V peak-to-peak ($P_{on} = 22.5$ mW) CP (light green). Next, the IP are applied with $T_{on} = 0.5$ s and $T_{off} = 0.5$ s (green), resulting in rapid oscillations of viscosity and formation of a viscosity metafluid. Following this, the suspension is fully dethickened by applying 10-V peak-to-peak ($P_{on} = 250$ mW) CP (light orange). When the IP with $T_{on} = 0.5$ s and $T_{off} = 0.5$ s are applied in this state (orange), the viscosity does not oscillate. This portion of the phase space does not support a viscosity metafluid, but simply an acoustically dethickened state (see SM [34] for discussion on fully dethickened states). The zoomed-in views (top) show the viscosity response for two cycles of the IP. (b) Schematic of the input voltage waveform for the acoustic protocol. (c) Tunability of the viscosity metafluids. The plot shows oscillations of viscosity with the time period T of IP. Purple and orange triangles show the average maximum and minimum of the oscillatory viscosity during IP. The hand-drawn grey curve illustrates the oscillations of viscosity. The on and off durations of the IP are kept equal and specified by $T_{on} = T_{off} = T/2$. The power of IP during the on-time (P_{on}) is set to 125 mW. Green and orange squares show the viscosity level obtained from CP of powers $P_{on} = 62.5$ mW and $P_{on} = 125$ mW, respectively. The viscosity oscillations at $T = 5$ ms are comparable to the sensitivity of our rheometer, thus we plot the average viscosity instead of the maximum/minimum viscosity for this condition. The measurements are performed at a constant strain rate $\dot{\gamma} = 0.57\ \mathrm{s}^{-1}$.

and a partially dethickened state, indicating the formation of a viscosity metafluid [green region in Figs. 2(a) and 2(b)].

To illustrate the remarkable tunability of these materials, we generate metafluid states with roughly the same average, but vastly different ranges of maximum and minimum viscosities [Fig. 2(c)]. Specifically, we vary the time period of the intermittent perturbations (IP), keeping $T_{on} = T_{off}$, and plot the envelope of the viscosity oscillations with the maximum indicated by purple inverted triangle and minimum indicated by the orange triangles. When the period of the acoustic perturbations is short (5 ms), the amplitude of the viscosity oscillations (illustrated schematically by the grey curve) is small. Here, the minimum and the maximum viscosity remain close to the value obtained when continuous acoustic perturbations are applied at half the power (green square). This behavior suggests that a timescale of 5 ms is too short for force chains to evolve at this shear rate [42]. As the period of acoustic perturbations is increased, the amplitude of the viscosity oscillations increases dramatically, with a viscosity maximum that approaches the fully thickened state (purple circle) and minimum that is comparable to the lowest viscosity attainable at this applied acoustic power (orange square). Importantly, we can access all the viscosities within this range (grey-shaded region). Thus, by varying the acoustic power as well as the periods T_{on} and T_{off}, one can easily generate oscillations over the entire range of viscosities associated with thickening, all while the fluid is continuously sheared.

B. Parameter space governing viscosity metafluids

To illustrate the broad range of parameters over which acoustically generated viscosity metafluids can be accessed, we determine the threshold strain rates and periods T_{off}, beyond which it is possible to attain metafluid states. Crucially, to obtain metafluid states, the strain rate must be sufficiently high for the suspension to thicken via formation of force chains during the period where the acoustics are off, T_{off}. For example, a strain rate of $\dot{\gamma} = 0.44\ \mathrm{s}^{-1}$ is insufficient to produce viscosity oscillations when the suspension is fully dethickened and intermittent perturbations with $T_{off} = 0.5$ s are applied {Fig. 2(a) orange shading; see SM [34] for details on fully dethickened states}. To determine the threshold strain rate for each T_{off}, we note that in the metafluid state the time-averaged viscosity under continuous acoustic perturbations

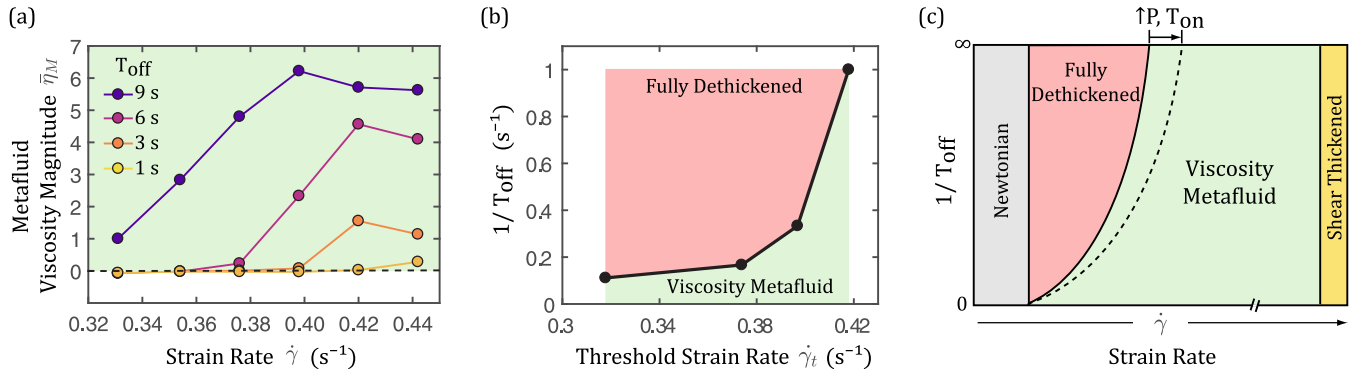

FIG. 3. Parameter space governing the formation of viscosity metafluids. (a) Metafluid viscosity magnitude $\bar{\eta}_M$, defined as normalized difference between the time-averaged viscosities under intermittent perturbations and continuous perturbations $(\bar{\eta}_{IP} - \bar{\eta}_{CP})/\bar{\eta}_{CP}$, as a function of strain rate $\dot{\gamma}$ and off times T_{off}. The viscosity metafluid region is depicted by the green color and the fully dethickened state is depicted by the dashed-black line. These measurements are performed at $T_{\text{on}} = 1$ s and $P_{\text{on}} = 250$ mW. (b) Phase boundary between the fully dethickened and viscosity metafluid regions. The threshold strain rate $\dot{\gamma}_t$ is defined as the maximum strain rate at a given T_{off} for which $\bar{\eta}_M \simeq 0$. (c) Phase diagram illustrating the viscosity metafluid region in $1/T_{\text{off}}$ versus $\dot{\gamma}$ parameter space. The diagram is constructed for a constant P_{on} and T_{on}. The dashed line indicates how the phase boundary between the fully dethickened and viscosity metafluid regions shifts as dethickening energy increases because of increase in power (P_{on}) or duration (T_{on}) of the acoustics.

$\bar{\eta}_{CP}$ is always smaller than the time-averaged viscosity under intermittent acoustic perturbations $\bar{\eta}_{IP}$ whereas in the fully dethickened state, these viscosities are identical. Thus, for each value of T_{off} we measure the magnitude of metafluid viscosity $\bar{\eta}_M$ defined as the normalized difference of the time-averaged viscosities $(\bar{\eta}_{IP} - \bar{\eta}_{CP})/\bar{\eta}_{CP}$ (see Experimental Protocols in Appendix 3) and determine for $T_{\text{on}} = 1$ s and $P_{\text{on}} = 250$ mW the threshold strain rate beyond which it becomes greater than zero [Fig. 3(a)]. As expected, we find that as T_{off} decreases, a larger strain rate is necessary to generate the metafluid state [Fig. 3(b)].

Collectively, from these observations, we composed a qualitative phase diagram describing the region in the $1/T_{\text{off}}$ versus $\dot{\gamma}$ parameter space where viscosity metafluids can be generated [Fig. 3(c)]. At low shear rates, the viscosity is Newtonian (grey) and insensitive to acoustic perturbations. As shear thickening occurs at a constant stress (corresponding to a constant strain rate for a given volume fraction), we expect the boundary between the Newtonian and fully dethickened regime to be vertical. Similarly, we anticipate that at extremely high shear rates inaccessible in our rheology measurements, the applied power will be insufficient to dethicken the system and the viscosity reflects the fully thickened state (yellow), indicating a second, strain rate independent boundary [13]. At intermediate shear rates and finite values of T_{off}, the boundary between the fully dethickened (orange) and viscosity metafluid region (green) is governed by the interplay between acoustic perturbations and shear flows as measured in Fig. 3(b). Moreover, these boundaries can also be shifted with the acoustic power P_{on} and T_{on} (dashed lines). Importantly, at each point within the viscosity metafluid region, we can dramatically tune the viscosity envelope that characterizes the metafluid [Fig. 2(c)]. Specifically, by precisely controlling T_{off}, T_{on}, the acoustic power, and strain rate, vastly different combinations of the minimum, average, and maximum viscosity can be obtained. We note that these are independent parameters and that depending on the imposed flows there may be others including duty cycle, phase of acoustics relative to oscillatory driving shear etc. As such, acoustic perturbations enable us to access novel metafluid states over a broad range of parameters, with the potential to engineer responses that are impossible to achieve in conventional fluids.

C. Engineering unique properties using viscosity metafluids

We illustrate how the low and high viscosity states generated by turning the acoustic perturbations on and off can be used as building blocks to engineer a wide range of composite time-averaged *effective* viscosities. We oscillate the driving stress sinusoidally with a positive bias (resulting in a time-averaged stress of σ_{DC}) and apply acoustics to generate low viscosity states during selective points in the stress cycle [Fig. 4(a)]. In the absence of any applied acoustics, the strain rate follows the oscillations in the stress [Fig. 4(a), first column]. Here, the effective strain rate is positive, corresponding to a net positive strain and an effective large positive viscosity. When acoustics are applied in phase with the stress ($\theta = 0$), low viscosity states are generated while the suspension is flowing forward. As a result, a large amount of strain is accumulated in the positive direction and the suspension flows in the direction of average applied stress, displaying an effective large positive strain rate and effective low positive viscosity [Fig. 4(a), second column]. In contrast, if the acoustics are applied with a phase lag $\theta = \pi$, the low viscosity states are generated in the cycle while the suspension is flowing *backwards*. As a result, the magnitude of the strain rate is larger when the stress is negative as compared to when the stress is positive. Consequently, a larger negative strain is accumulated as compared to the positive strain [Fig. 4(a), third column]. In this scenario, we can achieve an effective negative strain rate and a time-averaged effective *negative* viscosity.

The full range of behaviors demonstrated by the average strain rate and the effective viscosities at different phase lags is shown in Figs. 4(b) and 4(c). In addition to the negative viscosity states observed when the phase difference is close to π, we can also find values of θ where the strain rate is

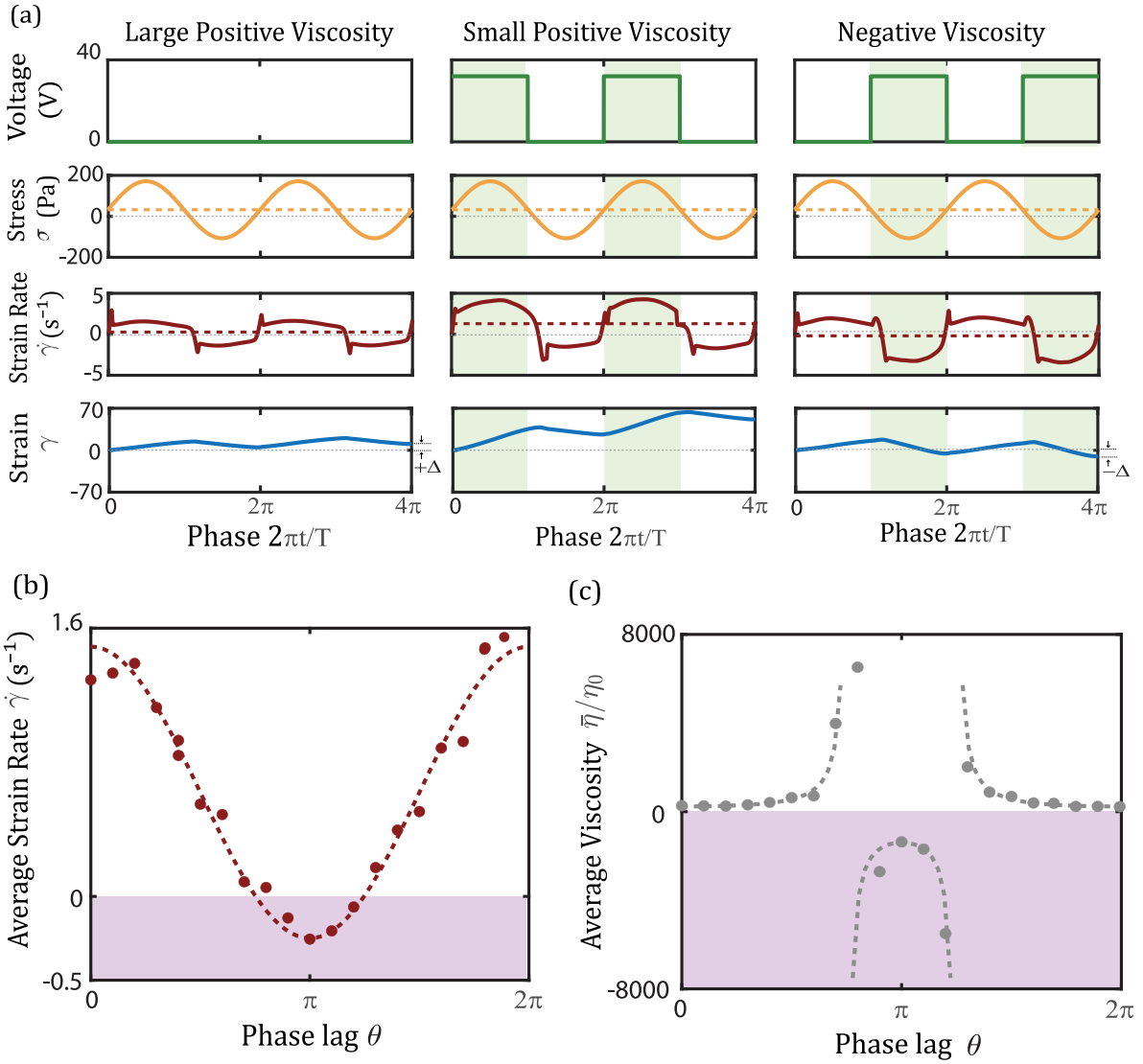

FIG. 4. A wide range of effective viscosities can be achieved in oscillatory systems by controlling the phase relation between shear and acoustics. (a) The applied voltage (first row) the applied stress (second row), strain rate (third row), and the net strain (fourth row) for three different acoustic conditions—no acoustics in the first column, acoustics in phase (phase lag, $\theta = 0$), and acoustics out of phase (phase lag $\theta = \pi$). An oscillatory stress (orange) with a positive bias (σ_{DC}, dotted line) is used to drive the sample. Acoustic perturbations with 40 V magnitude are applied at selective points in the cycle (green regions). The resultant strain rate (maroon) has an average (dashed-maroon line) that is small and positive in the absence of acoustics, large and positive when acoustics perturbations are applied in phase, and negative when acoustics perturbations are applied out of phase. Correspondingly, the net strain, indicative of the net motion of the sample is small and positive, large and positive and negative. (b) The time-averaged strain rate for various phase lags between the acoustics and applied stress. When acoustics is applied with a phase lag θ, the resultant average strain rate is nonmonotonic, and is well described by a $\dot{\gamma} = a(1 + b\cos\theta)$ dependence (dashed line). Interestingly, the strain rates are negative at phase lags close to π (purple region) (c) Time-averaged viscosities normalized by the solvent viscosity for various applied phase lags. The averaged viscosity $\bar{\eta}/\eta_0$ is well described by $(1 + b\cos\theta)^{-1}$ functional form (dashed line), which generates negative viscosity (denoted in purple) for phase lags near π.

zero, indicating the formation of states with infinite viscosity, where the suspension remains stationary, despite experiencing a net positive stress. Similar protocols can also be employed to engineer zero-viscosity systems (see SM [34]). Moreover, the range of achievable viscosities can be tuned by altering the exact protocols, the applied stresses and the acoustic power. We note that to achieve these extraordinary states we are pumping energy into the system via the acoustics and are therefore not violating any thermodynamic laws. Indeed, the instantaneous viscosity is always positive; it is only the time-averaged suspension response that can be tuned to be negative, zero or infinite. These results offer just a glimpse of the exotic behaviours displayed by viscosity metafluids achievable by simple manipulation of the shear and acoustic forces.

III. DISCUSSION

Our demonstration of generating arbitrary (negative, infinite, or zero) effective viscosities in the same material exemplifies the concept of a metafluid—the ability to de-

sign materials with time-averaged and spatially averaged bulk properties that are different from the spatial or temporal properties of the elements that make up the material. Here, we leverage our ability to temporally tune the viscosity to generate a composite fluid response, described by a time-averaged effective viscosity. We demonstrate that this can be done by simply changing the applied acoustic field relative to the driving shear forces (stress or strain rate).

Importantly, we are not claiming that the suspension itself is a metafluid. Rather, the different viscosity states (thickened or dethickened states) can be thought of as "building elements", and their *temporal* superposition can be thought of as mesoscale organization of building elements that generates an exotic macroscale response. This nontrivial temporal organization is what makes a simple suspension a programmable viscosity metafluid. This definition of a metafluid is analogous to, for example, photonic metamaterials where split ring resonators made of capacitors and inductors are configured to provide a temporal response to an incoming electromagnetic wave that temporally averages out to give a negative permeability and ultimately a negative index of refraction. In this system, one can now envision incorporating spatial programmability by designing an array of piezos, each locally and separately able to program the viscosity resulting in a spatially averaged viscosity metafluid response.

Notably, our approach is different from the superimposed shear flow protocols, which are used to *probe* material properties [43–46]. Instead, we use the phase between the acoustics and the driving shear to *tune* the material properties. Because these precise acoustic oscillation protocols require only that we attach a piezo at the boundary, achieving the demonstrated metafluid states should be straightforward even in complex flow geometries. Moreover, our approach is broadly applicable to any suspension whose instantaneous shear viscosity can be rapidly altered, including magneto- or electro-rheological fluids [47–49].

As such, viscosity metafluids open uncharted avenues for conveniently generating novel fluid flows, transient flow behaviors, and geometry-specific responses, all of which could be used in next-generation applications. For example, one can envision using acoustics to design instabilities for applications in mixing and improved heat and mass transfer. Other potential applications could include methods for processing dense coatings, generating hydrodynamic cloaking [6,50–55], and processing dense suspension in microfluidic environments during 3D printing [56].

ACKNOWLEDGMENTS

The authors would like to thank the Anton Paar VIP academic research program for providing the MCR 702 rheometer, and the Kirby group and Cohen group for valuable discussions. This work is supported by NSF CBET Grants No. 1804963, No. 1232666, and No. 1509308. I.C. was supported in part by NSF DMR Grant No. 2327094. C.N. acknowledges support from the Royal Academy of Engineering under the Research Fellowship scheme.

M.R. and P.S. contributed equally to this work. B.J.K., I.C., M.R., and P.S. conceived of experiments. E.Y.X.O., M.R., and P.S. performed experiments. M.R. and P.S. analyzed data. C.N. performed simulations. B.J.K., I.C., M.R., and P.S. wrote and edited the manuscript.

APPENDIX: MATERIALS AND METHODS

1. Materials and apparatus for experiments

We work with charge-stabilized, monodispersed colloidal suspensions consisting of 2-μm silica particles suspended in dipropylene glycol ($\eta = 0.11$ Pa s) at a volume fraction of $\phi \simeq 0.53$. The test setup consists of a piezoelectric disk bonded via epoxy to a custom-made aluminum bottom plate (details in [13]). The acoustic perturbations are generated by applying an AC voltage signal to the piezoelectric disk at resonance frequency $f = 1.15$ MHz corresponding to its thickness mode of vibration. For imaging the particle distributions in the presence of perturbations, the piezo-plate setup is integrated with a Zeiss 5 Live inverted confocal microscope, wherein the suspension is confined between the aluminum bottom plate and a glass slide. For measuring the rheological response in the presence of acoustic perturbations and shear, the piezo-plate setup is integrated with the Anton-Paar MCR 702 Rheometer. The glass top plate is used to apply steady shear to the suspension and measure the shear viscosity. The gap between the bottom plate and the top plate is set to 0.64 mm.

2. Protocol for simulations

We simulated the trajectories of $N = 2000$ spheres with radii a and $1.4a$ in a periodic box with length L chosen so that the volume fraction $\phi \equiv (2\pi/3)Na^3(1 + 1.4^3)/L^3 = 0.55$. Particles are subjected to hydrodynamic forces $\mathbf{F}_h = \mathcal{R}\mathbf{V}$ (where $\mathcal{R}$ is a resistance matrix comprising Stokes drag and pairwise lubrication terms); repulsive forces $\mathbf{F}_r = F_{r,0}\exp(-h\kappa)$ (with h the dimensionless surface-surface separation and $\kappa \approx 10^2$); and frictional contact forces $\mathbf{F}_c$ activated only when $h < 0$, and their trajectories are updated using a velocity Verlet scheme. We shear the simulation box at constant rate, and the suspension viscosity η/η_0 is controlled by $\dot{\gamma}/\dot{\gamma}^* = \dot{\gamma}\eta_0 a^2/F_{r,0}$. Further details are given in [57].

3. Protocol for measuring the magnitude of metafluid viscosity [Fig. 3(a)]

First, we preshear the suspension to achieve the steady state. Following preshear, we shear the suspension at a fixed strain rate for $t \simeq 60$ s. Concurrently, we apply continuous perturbations ($P_c = 250$ mW) for the first 20 s and then apply intermittent perturbations ($P_{on} = 250$ mW) of desired off-time for the next 40 s. We repeat this process for different strain rates and off times in a systematic manner, while keeping the P_{on} and T_{on} fixed. From the instantaneous viscosity response at each condition, we measure the time-averaged viscosities during the IP and CP, and calculate the magnitude of metafluid viscosity as $\bar{\eta}_M = (\bar{\eta}_{IP} - \bar{\eta}_{CP})/\bar{\eta}_{CP}$.

4. Protocol for generating different effective viscosities (Fig. 4)

First, we preshear the suspension to achieve the steady state. Following the preshear, we measure the viscosity at different stresses to identify the optimal mean stress, $\sigma_{DC} =$

34.8 Pa and the amplitude of the stress oscillations, $\sigma_a = 139.1$ Pa. We then apply a stress, $\sigma = \sigma_{DC} + \sigma_a \sin(2\pi t/T)$, where t is the time in seconds, and $T = 10$ s is the time period of the oscillations. Concurrently, we apply a square acoustic wave by simply turning the piezoelectric disk on and off at the appropriate points on the cycle. We repeat this process over a range of phase lags between the acoustics and the driving stress. We apply two stress oscillation cycles and average the stress, strain rate, and viscosity over both the cycles.

[1] L. R. Meza, A. J. Zelhofer, N. Clarke, A. J. Mateos, D. M. Kochmann, and J. R. Greer, Resilient 3D hierarchical architected metamaterials, Proc. Natl. Acad. Sci. USA **112**, 11502 (2015).

[2] V. M. Shalaev, W. Cai, U. K. Chettiar, H.-K. Yuan, A. K. Sarychev, V. P. Drachev, and A. V. Kildishev, Negative index of refraction in optical metamaterials, Opt. Lett. **30**, 3356 (2005).

[3] T. Han, X. Bai, J. T. L. Thong, B. Li, and C.-W. Qiu, Full control and manipulation of heat signatures: Cloaking, camouflage and thermal metamaterials, Adv. Mater. **26**, 1731 (2014).

[4] N. I. Landy, S. Sajuyigbe, J. J. Mock, D. R. Smith, and W. J. Padilla, Perfect metamaterial absorber, Phys. Rev. Lett. **100**, 207402 (2008).

[5] T. Brunet, A. Merlin, B. Mascaro, K. Zimny, J. Leng, O. Poncelet, C. Aristégui, and O. Mondain-Monval, Soft 3D acoustic metamaterial with negative index, Nat. Mater. **14**, 384 (2015).

[6] J. Park, J. R. Youn, and Y. S. Song, Hydrodynamic metamaterial cloak for drag-free flow, Phys. Rev. Lett. **123**, 074502 (2019).

[7] J. Park, J. R. Youn, and Y. S. Song, Fluid-flow rotator based on hydrodynamic metamaterial, Phys. Rev. Appl. **12**, 061002(R) (2019).

[8] J. Park, J. R. Youn, and Y. S. Song, Metamaterial hydrodynamic flow concentrator, Extreme Mech. Lett. **42**, 101061 (2021).

[9] S. A. Cummer, J. Christensen, and A. Alù, Controlling sound with acoustic metamaterials, Nat. Rev. Mater. **1**, 16001 (2016).

[10] O. Peretz, E. Ben Abu, A. Zigelman, S. Givli, and A. D. Gat, A metafluid with multistable density and internal energy states, Nat. Commun. **13**, 1810 (2022).

[11] A. Djellouli, B. Van Raemdonck, Y. Wang, Y. Yang, A. Caillaud, D. Weitz, S. Rubinstein, B. Gorissen, and K. Bertoldi, Shell buckling for programmable metafluids, Nature (London) **628**, 545 (2024).

[12] Y. A. Urzhumov, G. Shvets, J. Fan, F. Capasso, D. Brandl, and P. Nordlander, Plasmonic nanoclusters: A path towards negative-index metafluids, Opt. Express **15**, 14129 (2007).

[13] P. Sehgal, M. Ramaswamy, I. Cohen, and B. J. Kirby, Using acoustic perturbations to dynamically tune shear thickening in colloidal suspensions, Phys. Rev. Lett. **123**, 128001 (2019).

[14] M. M. Denn, J. F. Morris, and D. Bonn, Shear thickening in concentrated suspensions of smooth spheres in newtonian suspending fluids, Soft Matter **14**, 170 (2018).

[15] N. J. Wagner and J. F. Brady, Shear thickening in colloidal dispersions, Phys. Today **62**(10), 27 (2009).

[16] E. Brown and H. M. Jaeger, Shear thickening in concentrated suspensions: Phenomenology, mechanisms and relations to jamming, Rep. Prog. Phys. **77**, 046602 (2014).

[17] H. A. Barnes, Shear-thickening ("dilatancy") in suspensions of nonaggregating solid particles dispersed in newtonian liquids, J. Rheol. **33**, 329 (1989).

[18] N. Y. C. Lin, C. Ness, M. E. Cates, J. Sun, and I. Cohen, Tunable shear thickening in suspensions, Proc. Natl. Acad. Sci. USA **113**, 10774 (2016).

[19] R. Mari, R. Seto, J. F. Morris, and M. M. Denn, Shear thickening, frictionless and frictional rheologies in non-Brownian suspensions, J. Rheol. **58**, 1693 (2014).

[20] M. E. Cates, J. P. Wittmer, J.-P. Bouchaud, and P. Claudin, Jamming, force chains, and fragile matter, Phys. Rev. Lett. **81**, 1841 (1998).

[21] T. S. Majmudar and R. P. Behringer, Contact force measurements and stress-induced anisotropy in granular materials, Nature (London) **435**, 1079 (2005).

[22] M. M. Denn and J. F. Morris, Rheology of non-Brownian suspensions, Annu. Rev. Chem. Biomol. Eng. **5**, 203 (2014).

[23] E. Brown and H. M. Jaeger, The role of dilation and confining stresses in shear thickening of dense suspensions, J. Rheol. **56**, 875 (2012).

[24] M. Wyart and M. E. Cates, Discontinuous shear thickening without inertia in dense non-Brownian suspensions, Phys. Rev. Lett. **112**, 098302 (2014).

[25] N. Fernandez, R. Mani, D. Rinaldi, D. Kadau, M. Mosquet, H. Lombois-Burger, J. Cayer-Barrioz, H. J. Herrmann, N. D. Spencer, and L. Isa, Microscopic mechanism for shear thickening of non-Brownian suspensions, Phys. Rev. Lett. **111**, 108301 (2013).

[26] J. R. Royer, D. L. Blair, and S. D. Hudson, Rheological signature of frictional interactions in shear thickening suspensions, Phys. Rev. Lett. **116**, 188301 (2016).

[27] A. Singh, C. Ness, R. Seto, J. J. de Pablo, and H. M. Jaeger, Shear thickening and jamming of dense suspensions: The "roll" of friction, Phys. Rev. Lett. **124**, 248005 (2020).

[28] N. Y. C. Lin, B. M. Guy, M. Hermes, C. Ness, J. Sun, W. C. K. Poon, and I. Cohen, Hydrodynamic and contact contributions to continuous shear thickening in colloidal suspensions, Phys. Rev. Lett. **115**, 228304 (2015).

[29] D. Bi, J. Zhang, B. Chakraborty, and R. P. Behringer, Jamming by shear, Nature (London) **480**, 355 (2011).

[30] J. F. Morris, Lubricated-to-frictional shear thickening scenario in dense suspensions, Phys. Rev. Fluids **3**, 110508 (2018).

[31] R. Seto, R. Mari, J. F. Morris, and M. M. Denn, Discontinuous shear thickening of frictional hard-sphere suspensions, Phys. Rev. Lett. **111**, 218301 (2013).

[32] C. Ness, R. Mari, and M. E. Cates, Shaken and stirred: Random organization reduces viscosity and dissipation in granular suspensions, Sci. Adv. **4**, eaar3296 (2018).

[33] S. Pradeep, M. Nabizadeh, A. R. Jacob, S. Jamali, and L. C. Hsiao, Jamming distance dictates colloidal shear thickening, Phys. Rev. Lett. **127**, 158002 (2021).

[34] See Supplemental Material at http://link.aps.org/supplemental/10.1103/PhysRevResearch.6.043107 for discussion on measurement of structure factor in simulations, latency in fully

dethickened states, and generating effective viscosities with applied strain rate.

[35] C. Ness and M. E. Cates, Absorbing-state transitions in granular materials close to jamming, Phys. Rev. Lett. **124**, 088004 (2020).

[36] D. Hexner and D. Levine, Hyperuniformity of critical absorbing states, Phys. Rev. Lett. **114**, 110602 (2015).

[37] S. Wilken, R. E. Guerra, D. J. Pine, and P. M. Chaikin, Hyperuniform structures formed by shearing colloidal suspensions, Phys. Rev. Lett. **125**, 148001 (2020).

[38] S. Torquato and F. H. Stillinger, Local density fluctuations, hyperuniformity, and order metrics, Phys. Rev. E **68**, 041113 (2003).

[39] C. E. Zachary and S. Torquato, Hyperuniformity in point patterns and two-phase random heterogeneous media, J. Stat. Mech.: Theory Exp. (2009) P12015.

[40] R. Dreyfus, Y. Xu, T. Still, L. A. Hough, A. G. Yodh, and S. Torquato, Diagnosing hyperuniformity in two-dimensional, disordered, jammed packings of soft spheres, Phys. Rev. E **91**, 012302 (2015).

[41] S. Torquato, Hyperuniform states of matter, Phys. Rep. **745**, 1 (2018).

[42] Although at low Re, the *fluid physics* has no inherent timescale, there exist strain scales in the system corresponding to force chain formation or breakup. We refer informally to the timescale of the *system* as the ratio of the strain scale to the strain rate. This enables comparisons between the temporal manifestation of the strain scale and the time durations applied via acoustics.

[43] E. Y. X. Ong, M. Ramaswamy, R. Niu, N. Y. C. Lin, A. Shetty, R. N. Zia, G. H. McKinley, and I. Cohen, Stress decomposition in LAOS of dense colloidal suspensions, J. Rheol. **64**, 343 (2020).

[44] K. R. Lennon, M. Geri, G. H. McKinley, and J. W. Swan, Medium amplitude parallel superposition (MAPS) rheology. Part 2: Experimental protocols and data analysis, J. Rheol. **64**, 1263 (2020).

[45] K. Hyun, M. Wilhelm, C. O. Klein, K. S. Cho, J. G. Nam, K. H. Ahn, S. J. Lee, R. H. Ewoldt, and G. H. McKinley, A review of nonlinear oscillatory shear tests: Analysis and application of large amplitude oscillatory shear (LAOS), Prog. Polym. Sci. **36**, 1697 (2011).

[46] J. Ahmed, Advances in rheological measurements of food products, Curr. Opin. Food Sci. **23**, 127 (2018).

[47] Y. Z. Dong, Y. Seo, and H. J. Choi, Recent development of electro-responsive smart electrorheological fluids, Soft Matter **15**, 3473 (2019).

[48] J. R. Morillas and J. de Vicente, Magnetorheology: A review, Soft Matter **16**, 9614 (2020).

[49] M. Eshaghi, R. Sedaghati, and S. Rakheja, Dynamic characteristics and control of magnetorheological/electrorheological sandwich structures: A state-of-the-art review, J. Intell. Mater. Syst. Struct. **27**, 2003 (2016).

[50] Y. A. Urzhumov and D. R. Smith, Fluid flow control with transformation media, Phys. Rev. Lett. **107**, 074501 (2011).

[51] D. Culver and Y. Urzhumov, Forced underwater laminar flows with active magnetohydrodynamic metamaterials, Phys. Rev. E **96**, 063107 (2017).

[52] J. Park and Y. S. Song, Assembling hydrodynamic cloaks to conceal complex objects from drag, J. Fluids Struct. **98**, 103136 (2020).

[53] H. Pang, Y. You, A. Feng, and K. Chen, Hydrodynamic manipulation cloak for redirecting fluid flow, Phys. Fluids **34**, 053603 (2022).

[54] B. Wang, T.-M. Shih, L. Xu, G. Dai, and J. Huang, Intangible hydrodynamic cloaks for convective flows, Phys. Rev. Appl. **15**, 034014 (2021).

[55] E. Boyko, V. Bacheva, M. Eigenbrod, F. Paratore, A. D. Gat, S. Hardt, and M. Bercovici, Microscale hydrodynamic cloaking and shielding via electro-osmosis, Phys. Rev. Lett. **126**, 184502 (2021).

[56] R. E. O'Neill, J. R. Royer, and W. C. K. Poon, Liquid migration in shear thickening suspensions flowing through constrictions, Phys. Rev. Lett. **123**, 128002 (2019).

[57] O. Cheal and C. Ness, Rheology of dense granular suspensions under extensional flow, J. Rheol. **62**, 501 (2018).